# A New Approach to the Detection and Statistical Classification of $Ca^{2+}$ Sparks

Tamás Bányász,*† Ye Chen-Izu,*† C. W. Balke,*†‡ and Leighton T. Izu*†

*Institute of Molecular Medicine and the Departments of †Medicine and ‡Physiology, University of Kentucky, Lexington, Kentucky 40536

ABSTRACT The availability of high-speed, two-dimensional (2-D) confocal microscopes and the expanding armamentarium of fluorescent probes presents unprecedented opportunities and new challenges for studying the spatial and temporal dynamics of cellular processes. The need to remove subjectivity from the detection process, the difficulty of the human eye to detect subtle changes in fluorescence in these 2-D images, and the large volume of data produced by these confocal microscopes call for the need to develop algorithms to automatically mark the changes in fluorescence. These fluorescence signal changes are often subtle, so the statistical estimate of the likelihood that the detected signal is not noise is an integral part of the detection algorithm. This statistical estimation is fundamental to our new approach to detection; in earlier $Ca^{2+}$ spark detectors, this statistical assessment was incidental to detection. Importantly, the use of the statistical properties of the signal local to the spark, instead of over the whole image, reduces the false positive and false negative rates. We developed an automatic spark detection algorithm based on these principles and used it to detect sparks on an inhomogeneous background of transverse tubule-labeled rat ventricular cells. Because of the large region of the cell surveyed by the confocal microscope, we can detect a large enough number of sparks to measure the dynamic changes in spark frequency in individual cells. We also found, in contrast to earlier results, that cardiac sparks are spatially symmetric. This new approach puts the detection of fluorescent signals on a firm statistical foundation.

## INTRODUCTION

Rapid, two-dimensional (2-D) confocal microscopes allow surveying of large (~50 $\mu$m × 50 $\mu$m) regions at submicron resolution with high temporal resolution (~10 ms). These confocal microscopes coupled with an ever-increasing armamentarium of fluorescent probes provide unprecedented opportunities for probing the spatiotemporal dynamics of cellular processes. The underlying dynamics is marked by changes, often subtle, in the fluorescent signal of the probe. The challenge is to automatically detect these changes and to distinguish in a rigorous way noise from statistically significant fluorescence changes.

The need for automatic detection is more compelling for these 2-D confocals than with *x-t* linescans because changes in the fluorescent signals that may be obvious to the eye during rapid playback of the images seem to disappear when viewed frame-by-frame and because of the vastly greater volume of data produced by the 2-D confocals.

The detection algorithm we describe here differs in two important ways from the algorithm underlying the $Ca^{2+}$ spark detector pioneered by Cheng et al. (1) that we (2) and others (3) have modified. In these earlier algorithms, detection is based on differences in the fluorescence signals in space (or space-time in *x-t* scans). In the new detection algorithm, detection is based on differences in the 2-D images in time. This difference does not reflect a difference in philosophy but simply a means to accommodate our images that have important but static inhomogeneities, namely, transverse tubule (t-tubule) labeling. Differencing in time nulls these static structures but preserves the changing fluorescent signals.

The fundamental difference between our new approach and the earlier spark detectors lies in the classification of signals. In earlier algorithms, determining that the probability of a fluorescence change of a spark was due to processes that are independent of changes in $Ca^{2+}$ concentration (e.g., electronic noise, quantal Poisson noise) was incidental to detection. In the approach we take here, the probability assessment is fundamental to detection. We define a spark as the rejection of the null hypothesis that the fluorescence change is simply noise.

The early detectors have served well to remove the subjectivity of choosing sparks and they were reliable in detecting bright to moderately bright sparks. However, as we try to detect more subtle signals it is imperative that the detection and classification of signals be put on firmer statistical footing.

In this study, we developed the new detection and classification algorithms and used them to detect and measure $Ca^{2+}$ spark properties acquired using the high-speed, 2-D confocal microscope. Because we were able to detect a large number of sparks, including the dim sparks that would be difficult to detect by the earlier detectors, we could assess the dynamic changes in spark frequency in a single cell. One important finding is that cardiac sparks are spatially symmetric in contrast to earlier results (4,5).

*Submitted December 13, 2006, and accepted for publication February 12, 2007.*

Tamás Bányász and Ye Chen-Izu contributed equally to this work.

Address reprint requests to Leighton T. Izu, PhD, Biological and Biomedical Sciences Research Building, Rm. B257, 741 South Limestone St., Lexington, KY 40536-0509. Tel.: 859-323-6882; Fax: 859-257-3235; E-mail: LeightonIzu@uky.edu.

Dr. Bányász's permanent address is Medical and Health Science Center, University of Debrecen, Debrecen, Hungary.



0006-3495/07/06/4458/08 $2.00

doi: 10.1529/biophysj.106.103069

## METHODS

### Cell isolation

Male Sprague-Dawley rats (Harlan, Indianapolis, IN) were anesthetized with isoflurane supplemented with $O_2$. After suppression of reflexes, the hearts were removed via midline thoracotomy and a standard enzymatic technique was used to isolate the ventricular cells as described previously (6). All animals and procedures were handled strictly in accordance with the National Institutes of Health guidelines and our Institutional Animal Care and Use Committee approved protocols. Chemicals and reagents were purchased from Sigma-Aldrich (St. Louis, MO) if not specified otherwise.

### Indicator loading

The cells were loaded with Fluo-4 (Molecular Probes-Invitrogen, Carlsbad, CA) in physiological salt solution (PSS) containing (in mM): 145 NaCl, 4 KCl, 1 $CaCl_2$, 0.33 $NaH_2PO_4$, 1 $MgCl_2$, 10 HEPES, 10 glucose (pH 7.3, adjusted with NaOH), and 2.5 $\mu$M fluo-4 acetoxymethyl (AM) ester at room temperature for 45 min. 1-(3-sulfonatopropyl)-4-[beta[2-(di-*n*-octylamino)-6-naphtyl]vinyl] pyridinium betaine di-8 ANEPPS (Molecular Probes-Invitrogen), 15 $\mu$M, was added to the above solution in the last 15 min of the loading period to label the sarcolemma and t-tubules. The cells were studied within 2 h after loading.

### Confocal microscope

Experiments were carried out on the Zeiss 5 Live confocal microscope (Carl Zeiss, Jena, Germany) equipped with a 100× 1.4 numerical aperture plan-apo oil objective (Zeiss). The indicators were excited with a 488-nm laser and the emitted light was passed through a 520-nm long-pass filter. Images were scanned bidirectionally at 80 Hz. The zoom factor was set to 1, which produces an *x-y* pixel size of 0.12 $\mu$m × 0.12 $\mu$m.

### Preconditioning train

To achieve a uniform sarcoplasmic reticulum (SR) $Ca^{2+}$ load, cells in PSS were field stimulated (1 Hz) for 2 min, allowing ample time for the cell contraction to reach a steady state. Confocal image acquisition started 10 s after stopping field stimulation.

### Computation and data storage

The algorithms for the automatic detection, statistical classification, and analysis of $Ca^{2+}$ sparks are described in the Results section, below. These custom written programs are written using IDL (ITT Visual Information Solutions, Boulder, CO). The amount of data generated in a typical experiment (200 frames, 512 × 512 frame size, 12-bit pixel depth) is on the order of 100 MB. On an average day ~2 GB of data (20 cells × 100 MB) are produced. These data are stored on a 3-TB server that is backed up daily.

## RESULTS

$Ca^{2+}$ spark detection comprises two phases. In the first phase the spark detector detects the onset of a sufficiently large increase in fluorescence over a sufficiently large area. Whether this candidate spark will be classified as a spark must await the second phase where a statistical test on the signals is made.

### Preprocessing of images before spark detection

Before spark detection, a data set (series of tagged image file format files corresponding to an experiment) undergoes the following preprocessing steps:

1. The normalizing frame (see below) and the range of image frames that the spark detector will work on are chosen.
2. The image of the normalizing frame is rotated so that the long axis of the cell is horizontal. A grid (with user controllable spacing) is placed over the image to help align the t-tubules and the sarcolemma and get an accurate orientation angle $\theta$. All images within the range specified in Step 1 will be rotated by $\theta$.
3. The normalizing image is embedded in a large 2-D array of zeroes, rotated by $\theta$, and the region-of-interest is chosen. The embedding prevents the loss of the data image as a result of rotation.
4. Regions where the detection should not be carried out are chosen. A region could be excluded because it is not part of the cell (see the *bright triangular structure* near the top of Fig. 1 *A*) or because the t-tubules are highly skewed in that region. All this information is stored in a text file and read in during the spark detection.

### Phase 1: detection

An increase in the fluorescence signal at image frame $k$ is heralded by positive values in the difference image formed by subtracting the image on frame $k - 1$ from the image on frame $k$. Regions where the signals are unchanged are zero in the difference image. Although this is the basic algorithm for detecting sparks, the following steps are needed to make a practical spark detector.

#### *Normalization*

Each image (e.g., Image 6, Fig. 1 *B*) is normalized by division by a normalizing image (image 1, Fig. 1 *A*). For example, the normalization of image 6 (Fig. 1 *C*) is $N(6) =$ image 6/(image 1 + 1), where the division is carried out pixel by pixel. Adding 1 in the denominator avoids division by zero; the error incurred by doing this is insignificant since the mean baseline fluorescence value is ~500–1000. We will explain the rationale for normalization below. The normalizing frame is chosen by the user and is free of large increases in $Ca^{2+}$ (e.g., $Ca^{2+}$ waves) or obvious sparks. The normalized images are smoothed with a boxcar filter (9 × 9 kernel), which attenuates objects having spatial size of $<\sim$1.08 $\mu$m (9 × pixel size of 0.12 $\mu$m). Note that the prominent labeling of the t-tubules that are visible in panels *A* and *B* is not apparent in the normalized image.

#### *Differencing and thresholding*

The difference image of frame $k$ is $D(k) = N(k) - N(k - 1)$, where $N(k)$ is the $k$th normalized image (Fig. 1 *D*). Regions of constant brightness, which might be mistaken as sparks in a single image (in *red circles* in panels *A* and *B*), disappear

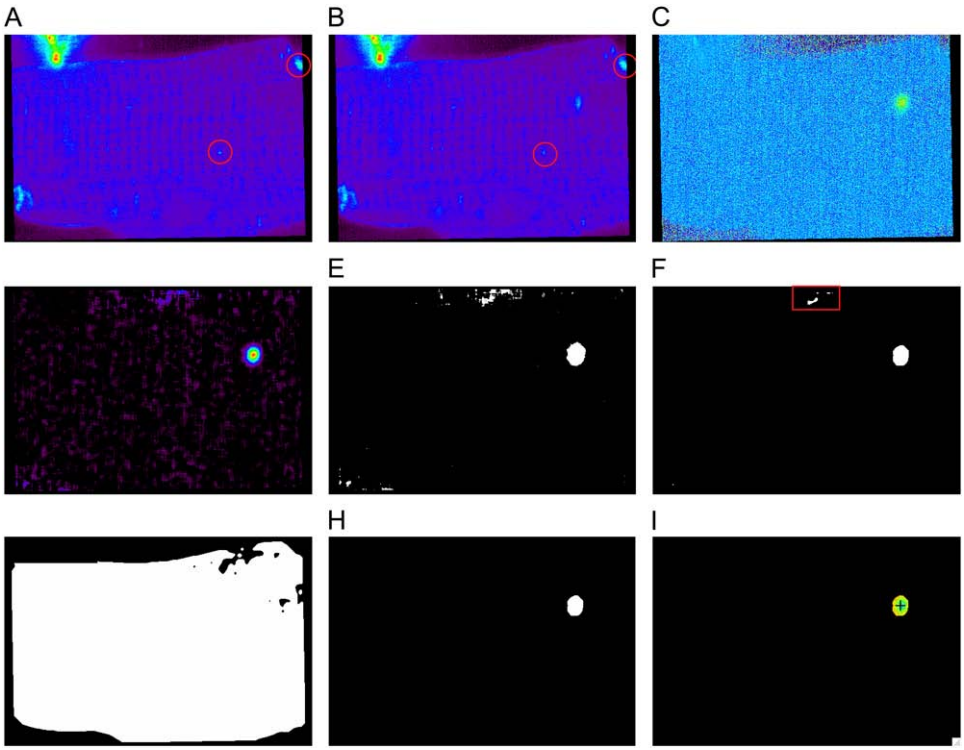


FIGURE 1 Steps in the first phase of spark detection. (*A*) Image used to normalize all other images. Bright, but constant, regions are circled. (*B*) The sixth image also has the bright constant regions (*circles*). (*C*) Image in *B* divided by the normalizer image. (*D*) The difference between sixth and fifth normalized image. (*E*) Results from setting pixels in difference that are $<0.075$–0 and all others to 1. (*F*) Live-or-die filtered image reduces or eliminates small regions that survive thresholding. Some pixels outside of the cell (*rectangles*) are still present. (*G*) Automatically determined extent of cell interior. (*H*) Results from multiplying images in *F* and *G*. The remaining white blob is the candidate spark. (*I*) The colored blob comes from multiplying the image in *H* with the raw 12-bit image shown in *B*. The candidate spark's center of mass coordinates are marked by the cross.

in the difference image. The binary image $B(k)$ (panel *E*) is made by setting all pixels of $N(k)$ greater than Threshold $=$ 0.075 to 1 and to 0 otherwise. Apart from the big blob near the right edge, there are a few isolated bright pixels within the cell (too small to be seen at this resolution) and many outside of the cell. In our epistemology, sparks are supposed to extend to micrometer size regions so regions of elevated fluorescence that are very small or where the density of bright pixels is low should not be regarded as sparks. Therefore, the ''live-or-die'' algorithm (2), which is designed to eliminate regions where the pixel density is low, is applied to $B(k)$. Panel *F* shows that the filter has eliminated all isolated pixels within the cell and most of the bright pixels outside of the cell. The live-or-die filter also consolidates isolated pixels in high-density regions, which reduces the likelihood of labeling a single spark as many small sparks. The live-or-die filter effectively combines the erosion and dilation operations (7) in a single step.

### *Automatic definition of the cell*

We need a way to automatically distinguish the inside of the cell from the outside. By defining what is inside, we can eliminate those bright pixels outside the cell that survive the live-or-die filtering (*rectangle* in panel *F*). To automatically define the cell, all pixels of the normalizing image less than the median value of the image are set to zero and one otherwise, and the live-or-die filter is applied to this binary image. The result is the white region in panel *G*. There are a few holes in the cell (corresponding to dim regions in the original image) but the automatically computed definition of the cell is adequate for eliminating the bright pixels that clearly lie outside of the cell. Additionally, the number of bright pixels multiplied by the pixel area gives the cell area. The cell area is needed to normalize the spark frequency (discussed below). The bright triangular region in the upper left hand part of panels *A* and *B* will show up as part of the cell. However, in the preprocessing stage, this region is marked and automatically expunged from the region defined as the cell.

### *Finding the spark coordinates*

Multiplication of the images in panels *F* and *G* gives the locations of the candidate sparks (the *white blob* in panel *H*). Each blob (a topologically connected region) is numbered. The candidate spark is isolated by multiplying the image in panel *H* with the original 12-bit image (panel *B*); see panel *I*. The coordinates of the center of mass of the spark (*cross* in panel *I*) are calculated from this isolated spark.

The center of mass coordinates are the main products of the spark detection algorithm. Other important data that are recorded are the area of the cell, a rough estimate of the area of the spark measured by the blob size, the frame number in which the spark appeared, and the blob number. These data uniquely identify each candidate spark.

## Normalization

In most of our experiments with ventricular cells we use di-8 ANEPPS to label the t-tubules (seen as in *A* and *B* of Fig. 1)

in addition to the $Ca^{2+}$ indicator. This helps us to accurately orient the cell so that the $x$ and $y$ center of mass coordinates are rationally related to the longitudinal and transverse axes of the cell. Because sparks originate on t-tubules (8), the sparks appear elongated along the t-tubule as seen in panel *B* in Fig. 1 and in the zoomed image of Fig. 2 *A*. The corresponding region of the normalizing frame is shown in panel *B*. Division of the raw image by the normalizer produces a more circular spark (Fig. 2 *C*). This circular spark shape is not an artifact of the normalization since sparks recorded in the absence of di-8 ANEPPS also have a circular shape (Fig. 2 *D*; (compare also Fig. 5, *A* and *B*).

## Phase 2: statistical classification of candidate sparks

The detected sparks ''look like'' sparks in terms of amplitude, spatial size, and pixel density. However, it is possible that the fluorescence increase that has been labeled as a spark could have arisen simply from random sources such as photon noise or shot noise that are independent of changes in the $Ca^{2+}$ concentration. Here we describe our statistical sieve to distinguish ''false sparks'' (those statistically indistinguishable from noise) from ''true sparks''. This sieve makes this distinction based on the probability that the observed fluorescence increase on frames $k$ and $k + 1$ was due to chance given the statistical properties of the signal before frame $k$. Fig. 3 illustrates how the statistical test is done. Let the coordinates of the center of mass of the candidate spark occurring on frame $k$ be $(x, y)$. Let the fluorescence values averaged over a $3 \times 3$ box centered on $(x, y)$ at frame $j$ be $F(j)$. The sample population from which we calculate the signal's statistical properties are frames $k - 6, k - 5, \ldots, k - 2$ (Fig. 3). We calculate the sample mean ($m$) and standard deviation ($s$) from these five samples. The probability that the fluorescence increases equal to the amplitude of the candidate spark, $F(k)$, occurred by chance given $m$ and $s$ is computed from the Student's $t$-distribution. If the probability of an increase of that magnitude by chance is less than $\alpha = 0.01$, then the fluorescence increase is tentatively considered to be a true spark. The candidate spark must pass another statistical test to further guard against false positives. We demand that the probability of a fluorescence increase on frame $k + 1$ is due to chance be less than $\beta = 0.025$. If this is so, then the candidate spark is labeled a ''true'' spark. The reason we relax the statistical stringency for the $k + 1$st point is because the spark is expected to decay between frames, which typically is 12 ms. If we retained the same stringency for the $k + 1$st point as the $k$th point, many events intuitively classified as sparks would not pass through the statistical sieve. The spark amplitude, $\Delta F/F_0$, is defined as $(F(k) - m)/m$.

The reason for not using the fluorescence value of frame $k - 1$ in calculating the sample mean and standard deviation is because it frequently happens that $F(k - 1)$ is already large relative to the previous five values, as shown in Fig. 3. If $F(k - 1)$ were used then the sample mean and standard deviation would be so large that many ''real sparks'' would not pass through the sieve.

This novel statistical sieving method has a number of features that merit emphasis. First, the sieving criteria—the choice of values for $\alpha$ and $\beta$, the exclusion of the $k - 1$ point, and the inclusion of the $k + 1$ point—are based on experience of what a spark is. However, once these parameters are set we know a priori the probability that the fluorescence increase seen is simply due to chance. Second, the population sample on which the signal's statistical properties are based is local to the candidate spark; that is, $m$ and $s$ are not calculated from the whole frame but just in the local neighborhood of the candidate spark. Thus an accurate calculation of probabilities is less affected by spatial inhomogeneities.

## Dynamic spark frequency

Because the 2-D confocal surveys such a large portion of the cell, in most cases there are enough sparks occurring per unit time to enable us to measure the dynamic changes in spark frequency in a single cell. We measured $Ca^{2+}$ sparks in 77 ventricular cells from four rats using the stimulation and recording protocol described. The time-dependent spark frequency is found by plotting the cumulative spark number

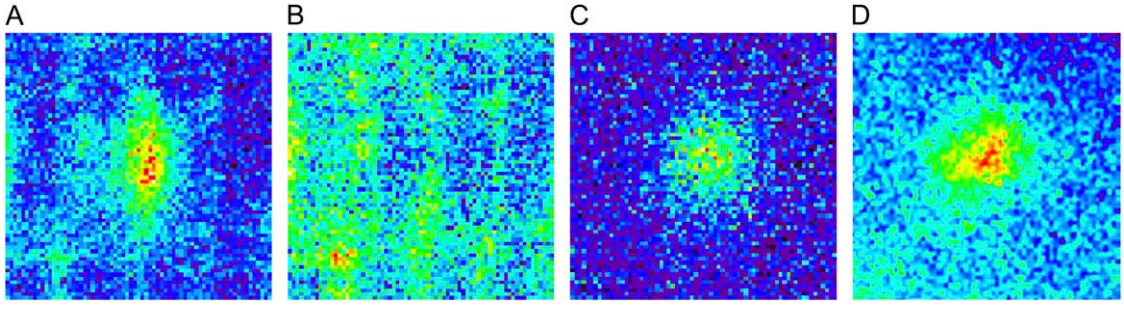


FIGURE 2 Effect of normalization. (*A*) Sparks in the raw images (nonnormalized) appear elongated along the t-tubule because of the presence of di-8 ANEPPS. (*B*) The same section of the cell as the spark in the normalizing image. (*C*) After normalizing, the sparks appear circular. (*D*) The circular symmetry of the spark is not an artifact of normalization since a spark recorded without di-8 ANEPPS and without normalization appears circular. See also Fig. 5.

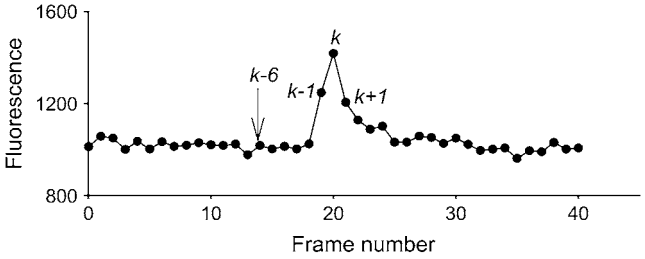


FIGURE 3 Statistical sieve. Data points used to calculate the probability that the fluorescence increases seen at the position of the candidate spark on frames $k$ and $k + 1$ are not due to chance fluctuations. See text for details.

against the product of time of occurrence and cell area. Examples from three cells are shown in Fig. 4 *A*. The linear increase of the cumulative spark number with space-time means that the spark frequency is constant. The spark frequency equals the slope of the best-fit line (*solid lines*). The spark frequencies are $3.65 \times 10^{-5}$ (*circles*), $2.48 \times 10^{-5}$ (*triangles*), and $7.29 \times 10^{-6}$/ms/$\mu$m$^2$ (*crosses*).

Two different kinds of dynamical spark frequency behavior are shown in Fig. 4 *B*. For the cell marked with *circles*, the cumulative spark number exhibits a quadratic behavior (*line*) meaning that the spark frequency is increasing linearly with time. From the quadratic fitting parameters, we deduce that the initial spark frequency was $4.28 \times 10^{-6}$/ms/$\mu$m$^2$ and the ''acceleration'' was $5.17 \times 10^{-12}$/ms$^2$/$\mu$m$^4$. The curve marked with crosses is an example of where the spark frequency did not behave in a simple way.

A total of 75% (58 of 77) of the cells had constant spark frequency, 8% (6 of 77) showed a linearly increasing spark frequency, and the remaining 17% (13 of 77) had either too few sparks to sensibly compute a spark frequency or the cumulative spark number had no readily interpretable shape (linear, quadratic, or exponential).

## Spark frequency distribution is skewed and broad

The vastly differing slopes in Fig. 4 *A* suggest a wide variation of spark frequencies between cells. Fig. 4 *C* shows the distribution of spark frequencies constructed from data only from cells that had constant spark frequency. The distribution of spark frequencies is highly left-skewed (most cells have low spark frequencies) but have a long tail (a few have very high spark frequencies).

We examined the spark frequency from each cell to see if the broad spark frequency distribution results from cells from one animal. We find the broad distribution of spark frequencies in cells from all animals. The spark frequencies range from $1.7 \times 10^{-6}$ to $1.3 \times 10^{-4}$/$\mu$m$^2$/ms; the mean is $2.2 \times 10^{-5}$/$\mu$m$^2$/ms; and the median is $1.2 \times 10^{-5}$/$\mu$m$^2$/ms.

To compare these values determined from sparks observed in 2-D images to spark frequencies determined from linescan images, we need to convert the various frequency units to a common unit of sparks/$\mu$m$^3$/ms. A common frequency unit is sparks/100 $\mu$m/s. Given that the lateral resolution of a confocal microscope is ~0.25 $\mu$m and the axial resolution is ~1 $\mu$m, each micrometer of a confocal scan samples a volume of ~0.25 $\mu$m $\times$ 1 $\mu$m $\times$ 1 $\mu$m = 0.25 $\mu$m$^3$. To convert our values to the common unit we multiply the values by 1/$\mu$m to account for the ~1 $\mu$m sampling depth along the optical axis. Some reported spark frequencies in various cells types are 0.85 sparks/100 $\mu$m/s $\rightarrow$ $3.4 \times 10^{-5}$/$\mu$m$^3$/ms (rat ventricular (5)); 4.6 sparks/100 $\mu$m/s $\rightarrow$ $1.8 \times 10^{-4}$/$\mu$m$^3$/ms

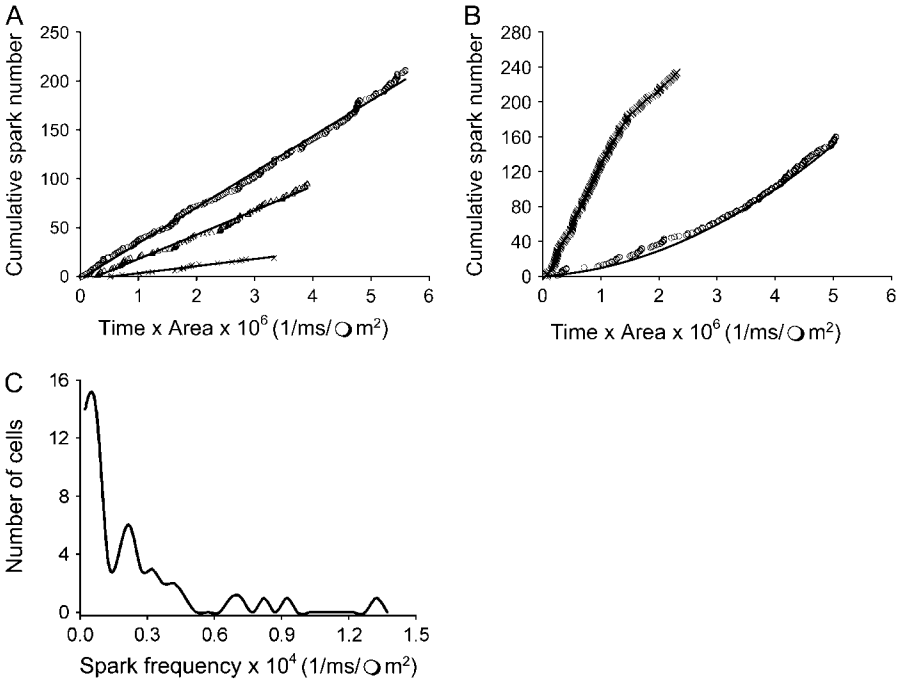


FIGURE 4 Dynamic spark frequency. (*A*) Example from three cells where the cumulative spark number increases linearly with space-time meaning that that spark frequency is constant. (*B*) In this cell, the cumulative spark number is fit to a quadratic function. The coefficient of the linear term is the initial spark frequency and the coefficient of the quadratic term is the ''acceleration''. (*C*) Distribution of spark frequencies, limited to only those cells that had constant spark frequency.

(rat ventricular (9)); $2.4 \times 10^{-6}$ to $1.2 \times 10^{-5}/\mu m^3/ms$ (rat atrial myocytes (10)); a maximum of $10^{-4}/\mu m^3/ms$ (cat atrial myocytes (11)); and ~70 sparks/pL/s→ $7 \times 10^{-5}/\mu m^3/ms$ (rabbit ventricular myocytes (12)). The broad range of spark frequencies covering 2 orders of magnitude we observed—$1.7 \times 10^{-6}$ to $1.4 \times 10^{-4}/\mu m^3/ms$—is comparable to the reported ranges, $2.4 \times 10^{-6}$ to $1.8 \times 10^{-4}/\mu m^3/ms$. Hüser et al. (11) also found that spark frequency varies greatly between cells.

The reason for the wide range of spark frequencies in cells from all animals we used is unclear. We sometimes observe very high spark frequency preceding myocyte hypercontraction and death. However, it is important to note that the frequencies used to construct Fig. 4 *C* are stable in the sense that the spark frequency in each cell was constant (Fig. 4 *A*). These data suggest that the heart contains myocytes whose spark frequency is stable within a cell but have large variation between cells.

### Sparks are spatially symmetric

The spatial extent of the sparks along the *x* (longitudinal) and *y* (transverse) axes is measured by the full width at half-maximum (FWHM) of the Gaussian function centered on the peak of the spark. To get a reliable Gaussian fit, we only used sparks that had amplitudes $\Delta F/F_0 \geq 0.2$ (907 sparks out of 6670 sparks), which puts the peak well above the noisy baseline. These cells were loaded with both fluo-4 and di-8 ANEPPS and images were normalized before analysis (see Fig. 2). The plot of each spark's FWHM along *y*, $FWHM_y$, and $FWHM_x$ is shown in Fig. 5 *A*. The points cluster about the 45° line of symmetry. The $FWHM_x$ is $2.32 \pm 0.008$ $\mu m$ (mean ± SE), and $FWHM_y$ is $2.30 \pm 0.007$ $\mu m$. There is no statistically significant difference between the mean values.

To test whether the symmetry of the sparks might be an artifact of normalization, we measured sparks in cells that were loaded with fluo-4 but without di-8 ANEPPS and we did not normalize the images. The FWHM was measured in 259 sparks. The plot of $FWHM_y$ and $FWHM_x$ shows a similar distribution around the line of symmetry (Fig. 5 *B*). The mean values along the *x* and *y* axes, $FWHM_x = 2.22 \pm 0.013$ $\mu m$ and $FWHM_y = 2.22 \pm 0.013$ $\mu m$, are identical. The sparks are symmetric, just as when the images are normalized, showing that the spark symmetry is not an artifact of normalization.

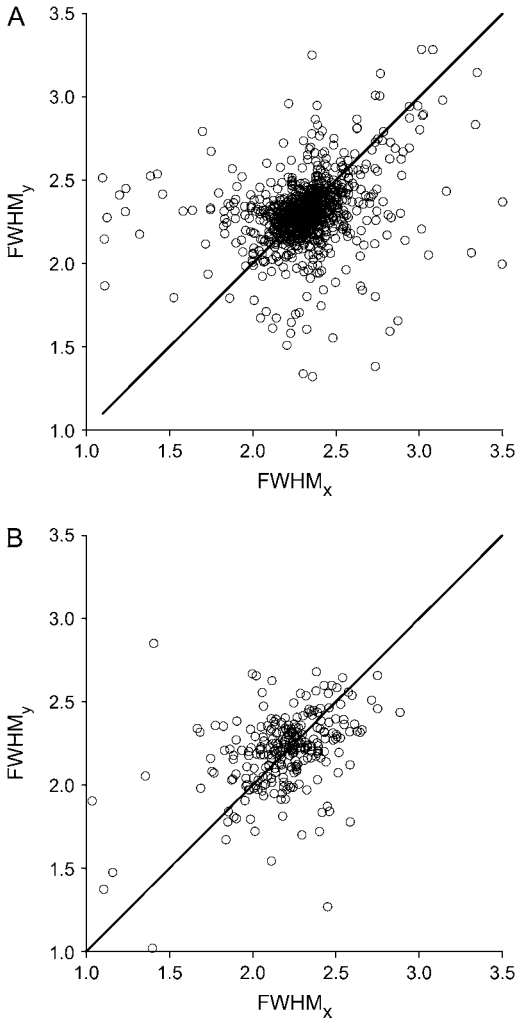


FIGURE 5 Spark FWHM along *x* and *y*. (*A*) The FWHM of sparks along *x* (longitudinal axis, $FWHM_x$) and *y* (transverse axis, $FWHM_y$) measured in cells colabeled with di-8 ANEPPS are symmetrically disposed around the 45° line. A total of 907 sparks from four animals were measured. (*B*) $FWHM_x$ and $FWHM_y$ measured in cells not colabeled with di-8 ANEPPS and without image normalization are also symmetrically disposed around the 45° line; 259 sparks from two animals were measured. The FWHM is given by $2\sigma(2\log 2)^{1/2}$, where $\sigma$ is the standard deviation from the Gaussian fit.

## DISCUSSION

### Spark epistemology and statistical sieves

Much of our understanding of cell biology—signaling, movement, and fertilization, for example—is due in large measure to the combination of fluorescent probes and confocal microscopy. The initial step in building this understanding is the detection of changes in the fluorescent signals. Since these detected fluorescence changes are often the groundwork for building models of cellular processes, it is imperative that we have a statistical estimate of the reliability of these fluorescent signals.

We have developed a new approach to the detection and statistical classification of fluorescence changes recorded by high-speed, 2-D confocal microscopes. In this new approach, detection comprises two phases. The first phase detects candidate sparks. In this phase the detector parameters are set to be liberal in what it accepts as candidate sparks. The second phase is a statistical sieve that separates ''false sparks'' from ''true sparks''. This classification is based on determining the probability the detected signal of that magnitude could have arisen from random fluctuation. In this phase, we

are conservative in what we accept as a spark. This second phase is fundamentally distinct from earlier $Ca^{2+}$ spark detectors that we and others have developed (1–3). In earlier spark detectors no attempt was made to explicitly calculate the probability that the candidate spark was a result of random signal fluctuations due, for example, to the quantal nature of light or electronic noise. Although the threshold for classification of sparks was based on the standard deviation of the background fluorescence, the actual threshold had no relationship to an a priori probability level. The threshold was chosen to capture what we thought sparks were and reject signals we felt were noise. Probability considerations were incidental. Even knowing that the threshold was $A$-fold greater than $\sigma$, where $\sigma$ is the standard deviation of the background signal, the signal probability based on this value might be inaccurate. This is because $\sigma$ is calculated for the whole image (after candidate sparks are removed) and this value may be, and often is, quite different from the local signal properties of the candidate spark. The statistical sieve described here uses the signal properties local to the candidate spark. An important consequence of using the local signal properties is that the sieve is less likely to misclassify a candidate spark when the background is changing. In this case, the standard deviation is large and the magnitude of the fluorescence increase of the candidate spark needs to increase correspondingly to qualify as a true spark.

This statistical classification of signals is especially important when the magnitudes of the events being detected are close to the level of the background. Important insights often come from the analysis of these subtle events. For example, by correcting for missed sparks (very dim ones not picked up by the spark detector) Song et al. (1) showed that the spark frequency was independent of the $Ca^{2+}$ load of the sarcoplasmic reticulum.

The statistical sieve is (largely) agnostic. It makes no assumption of what a spark is. From the viewpoint of the statistical sieve, a spark is simply a signal for which we reject the null hypothesis that it could be generated by random fluctuations consistent with the statistical properties of the signal before the purported spark.

## Spark symmetry and its possible implications

Our measurements reveal that cardiac sparks are spatially symmetric; their FWHM values along the longitudinal ($x$) and transverse ($y$) axes are essentially identical ($\sim$2 $\mu$m; Fig. 5). This observation differs from earlier findings (4,5) that cardiac $Ca^{2+}$ sparks were narrower along the transverse ($y$) than along the longitudinal ($x$) axis. However, there appears to be considerable difference in the magnitude of this asymmetry in these earlier reports. Although Parker et al. (4) do not give a measure of the asymmetry of the sparks, the spark images they present suggest a very marked asymmetry, which is supported by their estimate of a 2:1 ($x$:$y$) the diffusional anisotropy of the $Ca^{2+}$-bound fluo-3. Cheng et al. (5) find a more modest spark asymmetry where $FWHM_y$ is just 18% smaller than $FWHM_x$. Spatially symmetric sparks are seen in frog skeletal myocytes in the absence of caffeine but become elongated along $y$ when caffeine is present as neighboring $CA^{2+}$ release units trigger each other (3). If the image of the cell were randomly oriented when the FWHM along $x$ and $y$ were calculated, then the intrinsic asymmetry of the spark would be averaged out and we would obtain equal FWHM values. However, this is an unlikely explanation for symmetric sparks we observed because the cell image was carefully aligned—using the edge of the cell and the t-tubule labeling by di-8 ANEPPS as guides—so that the cell's $x$ and $y$ axes were nearly horizontal and vertical. Although not all t-tubules could be aligned with the $y$ axis, the small deviations from verticality would not produce the averaging needed to produce symmetric spark images from intrinsically asymmetric sparks.

Another possible source of image distortion comes from the difference in data acquisition rates between the $x$ and $y$ directions. In the Zeiss 5 Live a whole line of fluorescence along $x$ is acquired at the same time but each successive $y$ position occurs $\sim$25 $\mu$s later (at a typical frame rate of 80 Hz and image size of $512 \times 512$). The magnitude of the distortion depends on the relative timescales of scanning a spark and spark lifetime, analogous to the ratio of the camera's shutter speed to the subject's motion timescale. Since the spark FWHM is $\sim$2 $\mu$m and the pixel size is 0.12 $\mu$m, it takes $\sim$0.4 ms to scan the entire spark. Because the typical lifetime of a cardiac spark is $\sim$30 ms, much slower than the scan time of the spark, each $xy$ image is a faithful representation of the spark's instantaneous shape. Thus for relatively slow cardiac sparks, spark shape distortion due to different $x$ and $y$ data acquisition rates is small and this difference cannot cause a spurious symmetrizing of asymmetric sparks.

The symmetry of sparks is important because it likely reflects the underlying diffusion of $Ca^{2+}$. Diffusional isotropy implies that the dense network of proteins at the $z$-line (13) does not have a measurable influence on $Ca^{2+}$ diffusion. In our previous models of $Ca^{2+}$ sparks and $Ca^{2+}$ waves (14–16) we have assumed that both $Ca^{2+}$ and the $Ca^{2+}$-bound fluo-3 diffuse anisotropically. The change from anisotropic to isotropic diffusion would affect the estimate of the $Ca^{2+}$ current through the ryanodine receptor cluster, $I_{SR}$. When the diffusion coefficient along $y$ and $z$ (along the microscope axis) is half that along $x$, the magnitude of $I_{SR}$ needed to produce a spark with a given $FWHM_x$ is $\sim$56% of what is needed to produce a spark of the same $FWHM_x$ when diffusion is isotropic. The reason is the spark is spherical in the latter case and has a larger volume than the ellipsoidal spark (16).

## SUMMARY

We have developed a new approach to the detection of $Ca^{2+}$ sparks in 2-D confocal images, in which the statistical sieving candidate sparks are an integral part of the detection

process. Having demonstrated that the new detection algorithms are successful in detecting $Ca^{2+}$ sparks, the principle of statistical sieving should be applicable to all forms of event detection.

This work was supported in part by National Institutes of Health grants K25HL068704 (L.T.I.), RO1HL071865 (C.W.B. and L.T.I.), and RO1HL68733 (C.W.B.), and American Heart Association Scientist Development Grant 0335250N (Y.C.).

## REFERENCES

1. Song, L.-S., M. D. Stern, E. G. Lakatta, and H. Cheng. 1997. Partial depletion of sarcoplasmic reticulum calcium load does not prevent calcium sparks in rat ventricular myocytes. *J. Physiol.* 503:665–675.
2. Izu, L. T., W. G. Wier, and C. W. Balke. 1998. Theoretical analysis of the $Ca^{2+}$ spark amplitude distribution. *Biophys. J.* 75:1144–1162.
3. Brum, G., A. González, J. Rengifo, N. Shirokova, and E. Ríos. 2000. Fast imaging in two dimensions resolves extensive sources of $Ca^{2+}$ sparks in frog skeletal muscle. *J. Physiol.* 528:419–433.
4. Parker, I., W.-J. Zang, and W. G. Wier. 1996. $Ca^{2+}$ sparks involving multiple $Ca^{2+}$ release sites along Z-lines in rat heart cells. *J. Physiol.* 497:31–38.
5. Cheng, H., M. R. Lederer, R.-P. Xiao, A. M. Gómez, Y.-Y. Zhou, B. Ziman, H. Spurgeon, E. G. Lakatta, and W. J. Lederer. 1996. Excitation-contraction coupling in heart: new insights from $Ca^{2+}$ sparks. *Cell Calcium.* 20:129–140.
6. Kirk, M. M., L. T. Izu, Y. Chen-Izu, S. L. McCulle, W. G. Wier, C. W. Balke, and S. R. Shorofsky. 2003. Role of the transverse-axial tubule system in generating calcium sparks and calcium transients in rat atrial myocytes. *J. Physiol.* 547:441–451.
7. Russ, J. C. 1999. The Image Processing Handbook. CRC Press, Boca Raton, FL.
8. Shacklock, P. S., W. G. Wier, and C. W. Balke. 1995. Local $Ca^{2+}$ transients ($Ca^{2+}$ sparks) originate at transverse tubules in rat heart cells. *J. Physiol.* 487:601–608.
9. Lukyanenko, V., and S. Gyorke. 1999. $Ca^{2+}$ sparks and $Ca^{2+}$ waves in saponin permeabilized rat ventricular myocytes. *J. Physiol.* 521:575–585.
10. Woo, S.-H., L. Cleeman, and M. Morad. 2003. Spatiotemporal characteristics of junctional and nonjunctional focal $Ca^{2+}$ release in rat atrial myocytes. *Circ. Res.* 92:e1–e11.
11. Hüser, J., S. L. Lipsius, and L. A. Blatter. 1996. Calcium gradients during excitation-contraction coupling in cat atrial myocytes. *J. Physiol.* 494:641–651.
12. Satoh, H., L. A. Blatter, and D. M. Bers. 1997. Effects of $[Ca^{2+}]i$, SR $Ca^{2+}$ load, and rest on $Ca^{2+}$ spark frequency in ventricular myocytes. *Am. J. Physiol.* 272:H657–H668.
13. Pyle, W. G., and R. J. Solaro. 2004. At the crossroads of myocardial signaling: the role of Z-discs in intracellular signaling and cardiac function. *Circ. Res.* 94:296–305.
14. Izu, L. T., W. G. Wier, and C. W. Balke. 2001. Evolution of cardiac calcium waves from stochastic calcium sparks. *Biophys. J.* 80: 103–120.
15. Izu, L. T., S. A. Means, J. N. Shadid, Y. Chen-Izu, and C. W. Balke. 2006. Interplay of ryanodine receptor distribution and calcium dynamics. *Biophys. J.* 91:95–112.
16. Izu, L. T., J. R. H. Mauban, C. W. Balke, and W. G. Wier. 2001. Large currents generate cardiac $Ca^{2+}$ sparks. *Biophys. J.* 80:88–102.